

ACTIVE REGION LOOPS: *HINODE*/EXTREME-ULTRAVIOLET IMAGING SPECTROMETER OBSERVATIONS

DURGESH TRIPATHI^{1,6}, HELEN E. MASON², BHOLA N. DWIVEDI³, GIULIO DEL ZANNA^{1,6}, AND PETER R. YOUNG^{4,5}

¹ University College London, Mullard Space Science Laboratory, Holmbury St. Mary, Dorking, Surrey RH5 6NT, UK; d.tripathi@damtp.cam.ac.uk

² Department of Applied Mathematics and Theoretical Physics, University of Cambridge, Wilberforce Road, Cambridge CB3 0WA, UK

³ Department of Applied Physics, Banaras Hindu University, Varanasi 221005, India

⁴ Naval Research Laboratory, Code 7673, Washington, DC 20375, USA

⁵ George Mason University, 4400 University Dr. MS 6A2, Fairfax, VA 22030, USA

Received 2008 July 31; accepted 2009 January 2; published 2009 March 24

ABSTRACT

We have carried out a study of active region loops using observations from the Extreme-ultraviolet Imaging Spectrometer (EIS) on board *Hinode* using 1'' raster data for an active region observed on 2007 May 19. We find that active region structures which are clearly discernible in cooler lines (≈ 1 MK) become “fuzzy” at higher temperatures (≈ 2 MK). The active region was comprised of redshifted emissions (downflows) in the core and blueshifted emissions (upflows) at the boundary. The flow velocities estimated in the two regions located near the footpoints of coronal loop showed redshifted emission at transition region temperature and blueshifted emission at coronal temperature. The upflow speed in these regions increased with temperature. For more detailed study we selected one particular well-defined loop. Downward flows are detected along the coronal loop, being stronger in lower-temperature lines (rising up to 60 km s^{-1} near the footpoint). The downflow was localized toward the footpoint in transition region lines (Si VII) and toward the loop top in high-temperature line (Fe XV). By carefully accounting for the background emission we found that the loop structure was close to isothermal for each position along the loop, with the temperature rising from around 0.8 MK to 1.5 MK from the close to the base to higher up toward the apex ($\approx 75 \text{ Mm}$). We derived electron density using well-established line ratio diagnostic techniques. Electron densities along the active region loop were found to vary from 10^{10} cm^{-3} close to the footpoint to $10^{8.5} \text{ cm}^{-3}$ higher up. A lower electron density, varying from 10^9 cm^{-3} close to the footpoint to $10^{8.5} \text{ cm}^{-3}$ higher up, was found for the lower temperature density diagnostic. Using these densities we derived filling factors in along the coronal loop which can be as low as 0.02 near the base of the loop. The filling factor increased with projected height of the loop. These results provide important constraints on coronal loop modeling.

Key words: Sun: activity – Sun: atmosphere – Sun: corona – Sun: fundamental parameters – Sun: transition region – Sun: UV radiation

Online-only material: color figures

1. INTRODUCTION

Magnetically dominated solar plasma consists of a variety of structures, such as active regions, coronal loops, X-ray bright points, coronal holes, etc. Anchored in the photosphere, coronal loops populate both active and quiet regions, and form the basic building blocks of the Sun’s atmosphere. The physics of all kinds of loops, therefore, holds the key to understanding coronal heating, solar wind acceleration, and the flow of mass and energy in the region. Despite extensive work on the development of theoretical modeling (see, e.g., Klimchuk 2006; Narain & Ulmschneider 1996, for a review) the energy source, structure maintenance, and mass balance in coronal loops are not yet fully understood. The ultimate solution of this problem requires precise measurements of physical plasma parameters such as flows, electron temperature, density, and filling factors in spatially resolved coronal structures. The measurement of the above-mentioned parameters has been performed using earlier spectrometers. However, the measurements were limited by spectral and spatial resolutions. Moreover, the simultaneous temperature coverage has always been an issue.

The Extreme-ultraviolet Imaging Spectrometer (EIS; Culhane et al. 2007) on board *Hinode* spacecraft provides an

excellent opportunity to measure these parameters in greater detail. In this paper, we have studied overall intensity and flow structure in an active region. Moreover, we have studied flows, electron temperature, density, and filling factor along a well-resolved quiescent active region coronal loop. The rest of the paper is structured as follows. In Section 2, we provide observations and data reduction. We present our results in Section 3 with a brief summary and conclusion in Section 4.

2. OBSERVATIONS AND DATA PREPARATION

The EIS (Culhane et al. 2007) on board *Hinode* is an off-axis paraboloid design with a focal length of 1.9 m and mirror diameter of 15 cm. It consists of a multitoroidal grating which disperses the spectrum on two different detectors covering 40 Å each. The first detector covers the wavelength range 170–210 Å and the second covers 250–290 Å providing observations in a broad range of temperatures (≈ 5.8 –6.7 MK). The EIS has four slit/slot options available (1'', 2'', 40'', and 266''). The EIS provides monochromatic images of the transition region and corona at a high cadence using a slot (wide slit). High spectral resolution images can be obtained by rastering with a slit.

The EIS observed an active region on the Sun’s disk center on 2007 May 19, using the observation sequence *AR_velocity_map*. This sequence uses the 1'' slit with an exposure time of 40 s with a delay of 12 s. The EIS raster used in this analysis started at 11:41:23 UT and finished at 16:35:01 UT. The left panel in

⁶ Present address is Department of Applied Mathematics and Theoretical Physics, University of Cambridge, Wilberforce Road, Cambridge CB3 0WA, UK.

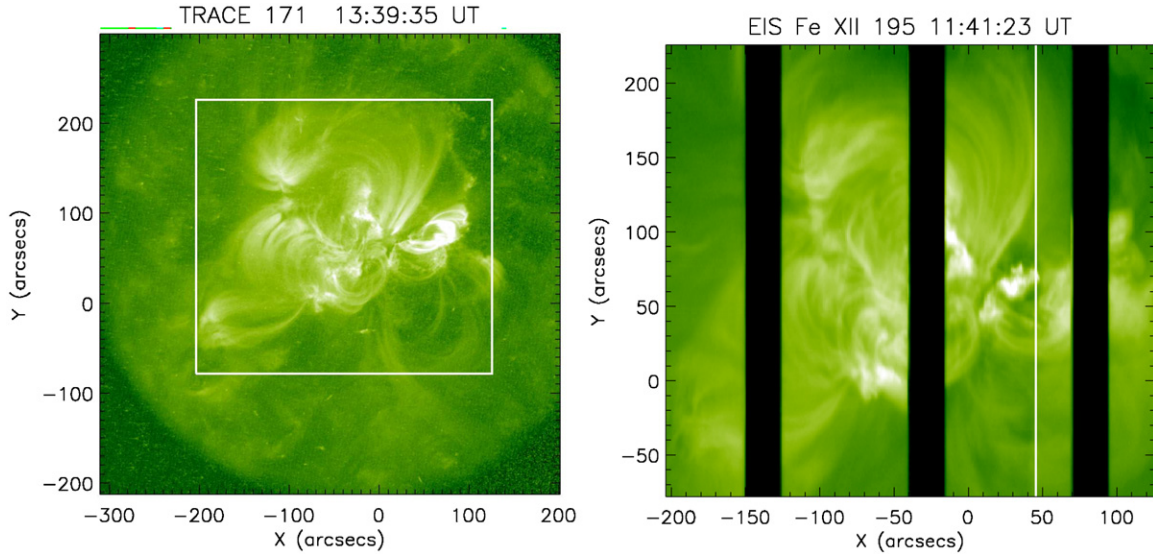


Figure 1. Left panel: *TRACE* $\lambda 171$ image showing a snapshot of the active region. The white box on the image demarks the region which was rastered by the EIS using the $1''$ slit. Right panel: EIS image in Fe XII $\lambda 195$. The black stripes represent the data gaps due to *Hinode* eclipses. The white straight line shows the location of the slit at 13:39:12 UT.

(A color version of this figure is available in the online journal.)

Figure 1 displays an image recorded by the *Transition Region and Coronal Explorer* (*TRACE*; Handy et al. 1999) in its 171 Å passband showing the complete active region taken at 13:39:35 UT. The overplotted box on the *TRACE* image represents the field of view (FOV) of the EIS raster. The right panel of Figure 1 shows an image recorded by the EIS in Fe XII $\lambda 195$. During this observation *Hinode* entered into eclipse mode 3 times, thereby causing data gaps. After the first eclipse, EIS observed a few well-resolved loop structures between $X = [0 : 50]$ arcsec. The white line demarks the slit location at 13:39:12 UT corresponding to the time of *TRACE* image shown in the left panel.

The sequence used for this study comprises very many useful spectral lines. For this particular study, we have only selected a few windows with lines such as Si VII $\lambda 275$ ($\log T[\text{K}] = 5.8$), Mg VII $\lambda 278$ and 280 ($\log T[\text{K}] = 5.8$), Fe VIII $\lambda 186$ ($\log T[\text{K}] = 5.8$), Fe X $\lambda 184$ ($\log T[\text{K}] = 6.0$), Si X $\lambda 258$ and 261 ($\log T[\text{K}] = 6.1$), Fe XII $\lambda 195$ and 186 ($\log T[\text{K}] = 6.1$), Fe XIII $\lambda 196$ and 203 ($\log T[\text{K}] = 6.2$), Fe XIV $\lambda 264$ and 274 ($\log T[\text{K}] = 6.3$), and Fe XV $\lambda 284$ ($\log T[\text{K}] = 6.4$). The selection of these lines provides diagnostics for the active region in a broad range of temperatures. The data were first processed using the standard processing routine *eis_prep.pro* provided in *Solar Software* (SSW) tree. We have fitted all the lines at each pixel of the EIS raster using the routine *eis_auto_fit.pro* which is also provided in SSW. Note that the Mg VII $\lambda 278$ and Fe XIV $\lambda 274$ are blended with an Si VII line. This blending issue is taken care of by using the branching ratios with Si VII $\lambda 275$. The Fe XIII $\lambda 203$ is blended with an Fe XII line which is taken care of by fitting two Gaussians. The two Fe XII lines $\lambda 195$ and $\lambda 186$ are self-blended and care must be taken while determining electron density using these line ratios (see Del Zanna & Mason 2005a; Young et al. 2007b).

It has been pointed out that images obtained from the two EIS detectors have an offset of about $20''$ in the Y (north–south) direction and about a couple of arcsec in the X (east–west) direction. Note that the EIS slit is oriented along north–south. Therefore, a co-alignment is necessary when comparing the outputs obtained from the two detectors. For this purpose we

have used images obtained at similar temperatures ($\log T[\text{K}] = 6.1$) from two CCDs (e.g., Si X $\lambda 261$ and Fe XII $\lambda 195$) and co-aligned them using a cross-correlation technique.

In order to derive physical parameters such as plasma flows, temperature, electron density, and filling factors, a number of different spectroscopic techniques can be applied to EIS observations. For a review on different spectroscopic techniques, see, e.g., Dere & Mason (1981) and Mason & Monsignori Fossi (1994).

The intensity of an optically thin emission line can be written as

$$I = A(z) \int_{T_e} G(T_e, N_e) \text{DEM}(T_e) dT_e, \quad (1)$$

where $A(z)$ is the elemental abundance, T_e is the electron temperature, and N_e is the electron density. $G(T_e, N_e)$ is the *contribution function* which contains all the relevant atomic parameters for each line, in particular the ionization fraction and excitation parameters. In quiet-solar conditions it is usually assumed that the ionization equilibrium holds and the $G(T_e, N_e)$ can be obtained using equilibrium ionization balance calculations. For this purpose, we have used CHIANTI version 5.2 (Dere et al. 1997; Landi et al. 2006). $\text{DEM}(T_e)$ is known as the *differential emission measure* which is defined as

$$\text{DEM}(T_e) = N_e^2 (dh/dT_e), \quad (2)$$

where dh is an element of column height along the line of sight (LOS).

To determine the average temperature along the LOS for a given point along the loop we have used the *EM-loci* method (see Del Zanna et al. 2002, and references therein). In this method, we plot the ratios of observed intensities with the contribution function $I_{\text{obs}}/(A(z)G(N_e, T_e))$ obtained using ionization balance calculations as a function of temperature. If the plasma is isothermal along the LOS then all the curves would cross at a single location indicating a single temperature. More precisely, this method is useful to find out if the plasma along the LOS is isothermal or multithermal.

The EIS wavelength bands were chosen to cover many density diagnostic lines (see, e.g., Del Zanna & Mason 2005b;

Young et al. 2007a, 2008; Tripathi et al. 2008b). We provide measurements of average electron density along the LOS using line ratios simultaneously from different line pairs. Once the electron densities have been estimated, the plasma filling factor (ϕ)—yet another important quantity—can be determined as (Porter & Klimchuk 1995; Cargill & Klimchuk 1997)

$$\phi = EM/N_e^2 h, \quad (3)$$

where EM is the total emission measure which is calculated by integrating over the width of the contribution function for a given spectral line, and h is the thickness of the loop along the LOS.

Obtaining the filling factor provides an indication of whether the loop structures are composed of multiple strands or not. Measuring the filling factors is very difficult due to the accumulated errors in estimating electron density, total emission measure (i.e., ionization equilibrium calculations), and the column depth. The main uncertainty, however, comes from the estimation of the column depth of the emitting plasma.

One of the main problems when studying the plasma parameters in coronal loops is to identify a loop which does not show substantial changes during the observing period. Investigating the observation sequence taken by the *TRACE*, we find that the well-defined loop structures seen after the first *Hinode* eclipse do not change significantly, at least within the time period when the EIS was rastering over them. Although there was a filament eruption at around 12:56 UT, one of the legs of which was rooted just west of the active region loops, the loops studied in this paper do not show any significant variations which could affect our study of the physical parameters. To be absolutely sure of this, we have also studied a raster by the EIS taken before the eruption (start: 09:42:12; end: 10:31:24 UT). We find that the loop structure has not changed from that raster to the one for which we have derived the physical parameters. We did not use the earlier raster to derive the physical parameters because the exposure time was short and therefore, we did not have enough counts for a good diagnostic study.

Since this study provides measurements of the physical parameters along a *quiescent coronal loop*, the results obtained can be reliably used as a benchmark against theoretical models of active region loops.

3. RESULTS

3.1. Overall Intensity and Flow Structure of the Active Region

One of the most important features of the EIS is to provide simultaneous observations at many different temperatures with an excellent spectral resolution ($\approx 3 \text{ km s}^{-1}$). This, therefore, helps us to enhance our understanding of the overall temperature structure and plasma flows in active regions.

Figure 2 displays the intensity (first and third rows) and the corresponding velocity maps (second and fourth rows) taken simultaneously at different wavelengths. The three black stripes in the intensity and velocity images are data gaps due to *Hinode* eclipse. It is evident from the intensity images (top row) that high-lying coronal loop structures are more prominent at cooler temperatures. The core of the active region is seen in high-temperature lines. The active region shape becomes more compact and bright at temperatures such as $\log T[\text{K}] = 6.3$ (Fe XIV) and $\log T[\text{K}] = 6.4$ (Fe XV). This implies that the core of the active region is hotter confirming previous observations by, e.g., Mason et al. (1999), Milligan et al. (2005), and

Tripathi et al. (2006) using data from the Coronal Diagnostic Spectrometer (CDS; Harrison et al. 1995) aboard the *Solar and Heliospheric Observatory* (*SOHO*; Domingo et al. 1995) and Tripathi et al. (2008a, 2008b) using EIS/*Hinode* observations.

The footpoint emission from the high-lying loops marked with the arrows in the top row images in Figure 2 are most intense in low-temperature lines such as Si VII (the top-left image in Figure 2) (and Fe VIII, not shown here) with little emission in high-temperature lines such as Fe XIII, Fe XIV, and Fe XV. This was also shown by Young et al. (2007a) using *Hinode*/EIS observations. The high-lying loop structures are best defined in the lower-temperature lines such as Fe X ($\log T[\text{K}] = 6.0 \text{ MK}$). The loop structures merge into the diffuse background emission with increasing temperature (see also Del Zanna & Mason 2003). In hot temperature lines such as Fe XV (and Fe XVI, not shown here) only the core of the active region remains visible.

In order to obtain the LOS velocity information (see the bottom rows in both panels of Figure 2), instrumental effects such as the EIS *slit-tilt* and spacecraft *orbital variation* have to be compensated for. It is known that the EIS slits are not vertical on the detectors (e.g., Young et al. 2007b). The $1''$ slit has a tilt of about $1.2 \times 10^{-6} \text{ \AA pixel}^{-1}$. Therefore, while deriving velocities, it is essential to compensate for this effect. This is done using the IDL routine *eis_slit_tilt.pro* provided in the SSW tree. After compensating for the slit-tilt, we applied a correction for the orbital variation using *eis_orbit_spline.pro* also provided in SSW. Exploring a large number of data sets, it has been concluded that the spacecraft orbital variation changes from one EIS study to another. Therefore, there is no automatic way to compensate for this effect and it has to be estimated for each and every study separately. To estimate the orbital variation, it is necessary to select a quiet region in the raster. By doing so, we ensure that we do not remove (add) any original (artifact) values from (to) the data. For this purpose, we selected the bottom 50 pixels in the quiet-Sun region in this raster. By studying the average variations of the line centroids, we could determine the effects of orbital variation. Applying the above-mentioned corrections, we obtained a corrected set of data, to enable us to estimate the Doppler shift in the coronal structures. To summarize, the “at rest” reference wavelength has been obtained by considering the bottom 50 pixels.

Based on the Solar Ultraviolet Measurement of Emitted Radiation (SUMER) measurements, Peter & Judge (1999) and Teriaca et al. (1999) found that the spectral lines show nonzero line shifts in quiet-Sun observations. The cooler temperature lines ($T < 0.5 \text{ MK}$) showed redshifted emission while the hotter lines ($T > 0.5 \text{ MK}$) were blueshifted. Ideally, while investigating the Doppler shift measurements this effect should be considered. However, we note that the above SUMER studies did not contain the spectral lines forming at temperature higher than $\log T[\text{MK}] = 6.1$. Therefore, this effect can only be taken in account for the line such as Si VII, Fe X, and Fe XII in our analysis and not for high-temperature lines studied in this paper such as Fe XIII, Fe XIV, and Fe XV. Since we are interested in comparing the flows observed in these lines with respect to each other, it is not worthwhile taking such effects into account for some lines but not for higher-temperature lines.

The bottom row images in Figure 2 show the derived Doppler velocity maps for different lines. The velocity maps are plotted in the range of $\pm 30 \text{ km s}^{-1}$. The velocity maps show redshifts and blueshifts all over the active region. The redshifts (downflows) are more prominent in the core region of the active region and

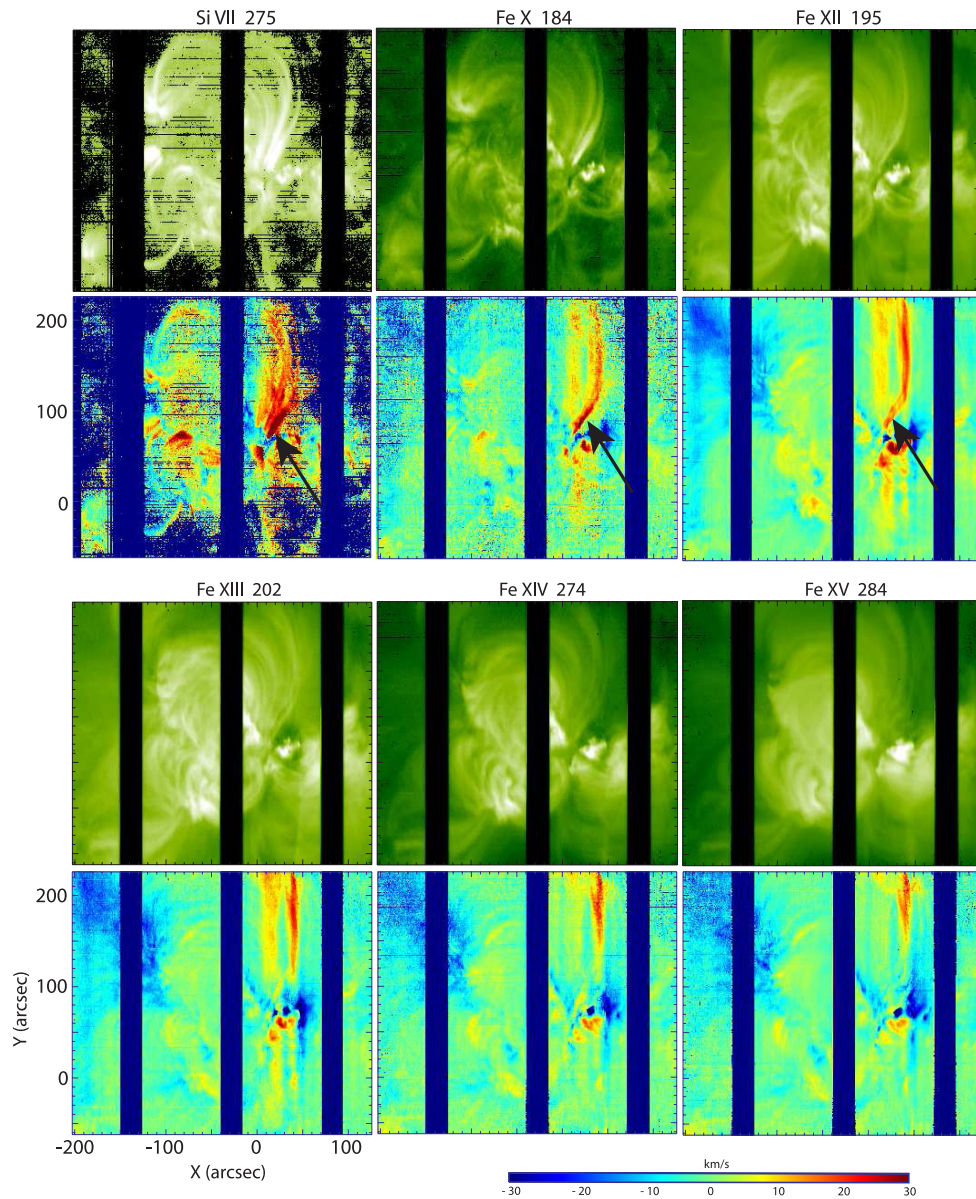


Figure 2. Intensity and the corresponding velocity maps obtained in Si VII, Fe X, and Fe XII (top panel) and Fe XIII, Fe XIV, and Fe XV lines (bottom panel). The arrows in the top panel velocity maps locate the spatially resolved coronal loops.

(A color version of this figure is available in the online journal.)

blueshifts (upflows) are more prominent at the boundary of the active region similar to the observations made by, e.g., Del Zanna (2008a, 2008b), Harra et al. (2008), Hara et al. (2008), and Doschek et al. (2008).

The plasma flow structures in high-lying loops are better defined at lower temperatures in a similar way to structures seen in the intensity maps. To compare the flow structure in a spatially resolved coronal loop, we have marked a chosen loop with an arrow in the velocity maps in the top panel of Figure 2. Plasma downflow is seen at all temperatures along the loop. However, downflows are localized toward the footpoint regions in cooler lines such as Si VII and Fe VIII (not shown in figure) and was as high as ($\approx 60 \text{ km s}^{-1}$). Similar results from SUMER have also been reported recently by Del Zanna (2008b), Dammasch et al. (2008), Marsch et al. (2008), and Curdt et al. (2008). Downflows are seen all along the loop in Fe X and Fe XII lines being stronger toward the footpoint region. At high temperatures such as $\log T[\text{K}] = 6.3$ (Fe XIV) and $\log T[\text{K}] = 6.4$ (Fe XV)

the downflows are stronger toward the loop top regions with almost no downflow signature at footpoints. We note that these velocities are along the LOS. Therefore, the actual velocities would be much higher than these values.

From the intensity and velocity maps, it appears that the region showing redshift in cooler spectral lines shows blueshift in high-temperature lines. To show this quantitatively we have selected two regions labeled “Region 1” and “Region 2” (see the top panel of Figure 3) and plotted the average velocities obtained at different lines (the bottom panel of Figure 3). These two regions are located at the footpoints of the high-lying coronal structures. As it is evident from the plot, in Si VII line both the regions show redshifted emission (downflows) turning to blueshifted emission (upflows) with increasing temperatures. We note that both the selected regions correspond to footpoint regions of coronal loop. Observation of blueshifted emission in high-temperature lines at the base of the coronal loops provides evidence of upflows in loops.

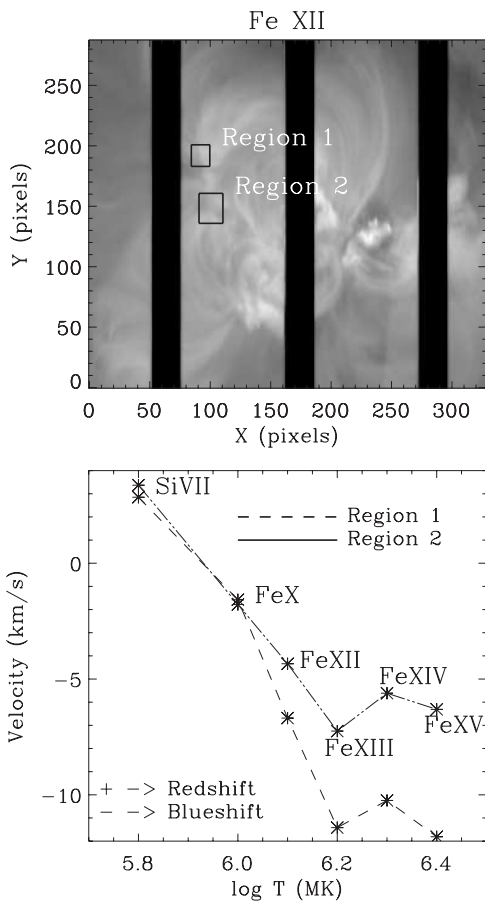


Figure 3. Top panel: Fe XII image. Two boxes labeled as Region 1 and Region 2 are chosen to measure the average velocity. Bottom panel: average velocities in Region 1 and Region 2 in different lines.

It is worth pointing out that if we take into account the results obtained from SUMER measurements (Peter & Judge 1999; Teriaca et al. 1999), the average downflows in Si VII would be weaker by about $\approx 3 \text{ km s}^{-1}$ and average upflows seen in Fe X and Fe XII would be stronger by about ≈ 4 and $\approx 9 \text{ km s}^{-1}$, respectively. However, we do not have measurements for other higher-temperature lines from SUMER to make such a comparison.

3.2. Intensity Variation Across Loop Structures

After the first *Hinode* eclipse, the EIS recorded a few very well-defined vertical loop structures (see Figure 1, right panel $X = [0 : 50]$ arcsec) before going into another eclipse. The orientations of these loops (almost north-south) are such that rastering across the loops does not take a long time (less than 20 minutes). Therefore, this loop system offers us an excellent opportunity to study the physical plasma parameters along active region loops at a given time. From now on we will only focus on the region $\approx X = [-10 : 65]$ arcsec and $\approx Y = [70 : 220]$. Note that the EIS rasters a region on the Sun from west to east.

Figure 4 (top panel) shows monochromatic images of the subregion from the EIS raster. The spectral lines for which these images were created are labeled for each frame. As is evident from the figure, the coronal loops in the active region are more sharply defined in the images observed at lower-temperature lines such as Si VII, Fe VIII, and Fe X than those in the higher-temperature lines such as Fe XII, Fe XIII, Fe XIV, and Fe XV. The structures in Si VII are the sharpest and are fuzziest in Fe XV.

The structures seen in Fe X are similar to those seen in the TRACE 171 Å image (see Figure 1, left panel). However, the small difference is due to somewhat better spatial resolution of TRACE ($1''$) than that of EIS ($3''\text{--}4''$).

The active region loop structures are clearly discernible in the Fe XII line. The images obtained in the Fe XIV and Fe XV lines lack clarity while noting that the loops seen in Fe XII line may have partial overlap with Fe XV line. Based on these observations it is plausible to conclude that the coronal structures are fuzzy at higher temperatures. This in itself has been a matter of debate among the solar physics community for many years (since Skylab days). The question concerns whether the solar corona really is fuzzy at high temperatures or simply appears to be fuzzy because the instrumental spatial resolution and line intensities are insufficient at higher temperatures. The high-temperature corona was observed with the soft X-ray telescope (SXT; Tsuneta et al. 1991) aboard *Yohkoh*, however cooler temperature emission could not be observed with *Yohkoh*. The SOHO/CDS instrument could observe the corona simultaneously at low temperatures ($\approx \log T[\text{K}] = 5.0$ MK) as well as high temperatures $\approx \log T[\text{K}] = 6.4$ MK. However, the CDS spatial resolution ($\approx 5''\text{--}6''$) was not enough to unambiguously resolve this issue. Similarly, with SOHO/EIT which could observe the Sun at low temperature using its Fe IX channel and at high temperature using the Fe XV channel but did not have sufficiently good spatial resolution.

To clarify this point, we chose a region (marked between the two horizontal white lines in the top panels of Figure 4) and plotted the corresponding intensity profile (summed in the Y-direction) in the bottom panels of Figure 4. It is straightforward to see that the intensity fluctuations due to the presence of spatially resolved coronal features are highly pronounced in low-temperature emission, but much less obvious at higher temperatures. The intensity images in Si VII and Fe X lines show a spike at location $X = 40$ which is basically due to a spatially resolved loop, marked by an arrow as loop “B.” Another active region loop “A” is also marked by the arrows in the Fe X image. For both these loops we can identify enhancements in the intensity profiles for lines such as Si VII and Fe X. However in the Fe XII image, the intensity corresponding to the loop “B” has almost disappeared in the fuzzy background, but the intensity enhancement corresponding to the loop “A” is still clearly discernible. The intensity fluctuation corresponding to the loop “A” is still just about discernible in Fe XIII and Fe XIV. However, Fe XV shows a sharp decrease in the intensity corresponding to the position of loop “A.” It is interesting to note that the intensity profile corresponding to the Fe XV line shows a dip for both the coronal loops marked “A” and “B.” However, it also shows a sharp enhancement (barely identifiable in lower panel plots) between these two dips where the intensity profiles corresponding to cooler lines show a dip. The plot also demonstrates the possible partial overlaps between the loop structures seen in Fe XII line and those seen in Fe XV line. This basically implies that active regions are comprised of coronal loops seen at different temperatures and intermingled with each other (see also Del Zanna et al. 2006).

3.3. Temperature Structure Along Loops: Isothermal or Multi-thermal?

One of the most important issues when studying the problem of active region heating and the coronal heating in general is whether the coronal loops are isothermal or multi-thermal along the LOS. This issue has been studied extensively using data

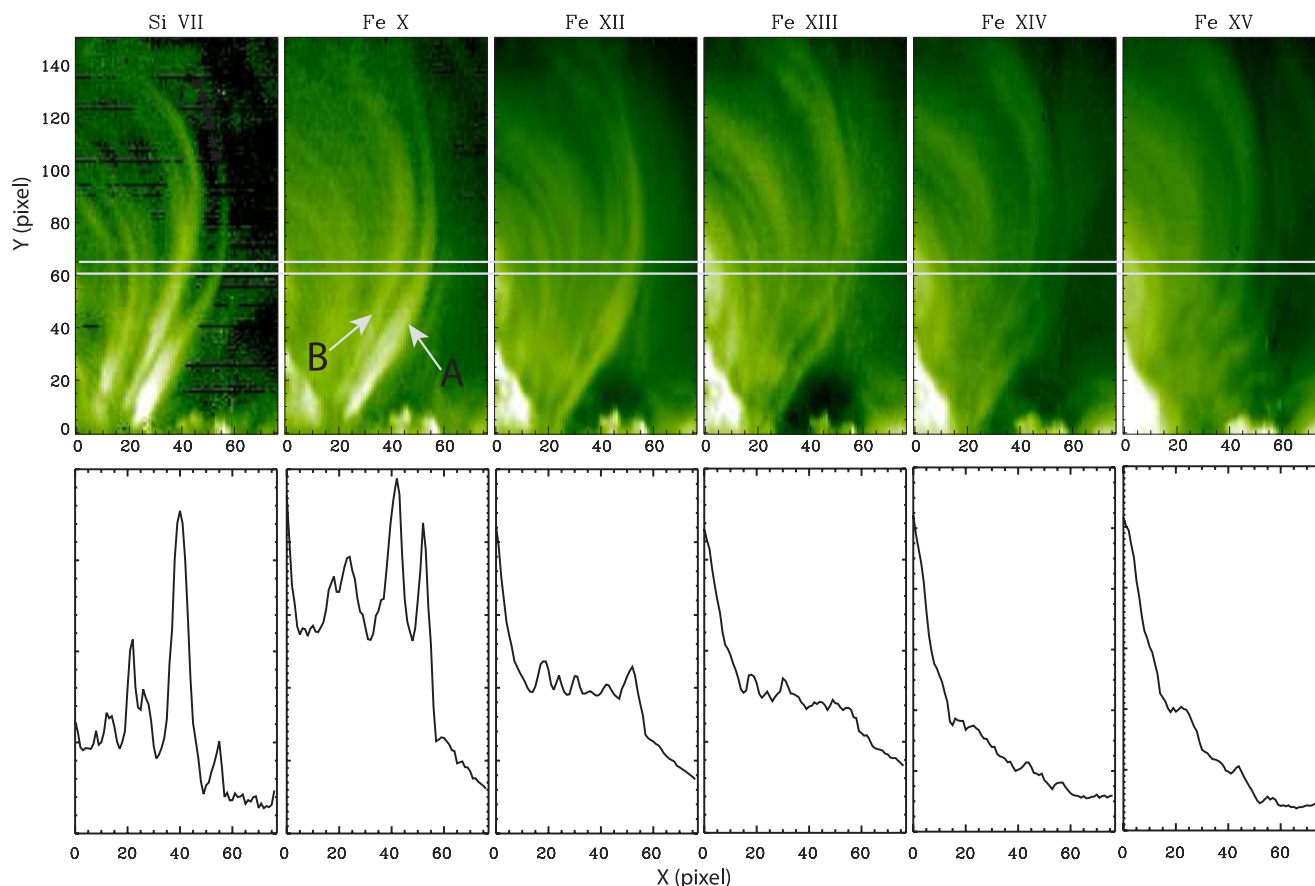


Figure 4. Top panel: the active region loops seen at different temperatures. Bottom panels: total intensity variation in the region marked by the two white lines in the corresponding top panels.

(A color version of this figure is available in the online journal.)

from *TRACE* (see, e.g., Aschwanden et al. 2001), and CDS (e.g., Schmelz et al. 2001; Del Zanna & Mason 2003; Schmelz et al. 2007). The main controversy started when using the spectroscopic techniques such as DEM, Schmelz et al. (2001) showed that the loops were not isothermal either along the loop length or along the LOS. Later on using an observation which was taken by *TRACE* and CDS simultaneously Del Zanna (2003) and Del Zanna & Mason (2003) (see also Cirtain et al. 2007) showed that the loops were isothermal along the LOS and the proper treatment of the diffuse background is important.

Given the excellent spatial resolution of EIS and the broad temperature coverage, we have estimated temperatures along the LOS at many given points along the loop length. For this purpose we have applied the *EM-loci* method using a set of spectral lines that are almost density insensitive. In the *EM-loci* method we plot $I_{\text{obs}}/(A(b)G(N_e, T_e))$ as a function of temperature. The contribution function $G(N_e, T_e)$ was calculated with CHIANTI version 5.2, using coronal abundances of Feldman (1992) with a density of 10^9 cm^{-3} and the ionization fractions of Arnaud & Rothenflug (1985). Similar results were obtained using the ionization fractions of Mazzotta et al. (1998).

It is evident from Figure 4 that the loops are not sharply defined at all temperatures. They are best seen at lower temperatures. Based on a visual inspection, therefore, we have chosen two loops, namely, loop A and loop B (labeled in Figure 5) in Fe X and used these as a proxy for other lines where the loops are not sharply defined. For the background subtraction we chose a loop-shaped structure running parallel to the loop B, shifted

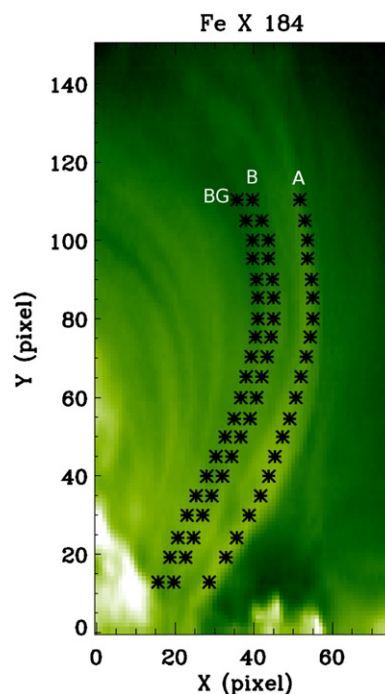


Figure 5. Image obtained in Fe X $\lambda 184$. The overplotted asterisks show the two loops and the background. The rightmost is loop A and the middle is loop B. The leftmost one, labeled as BG, is used for background subtraction.

(A color version of this figure is available in the online journal.)

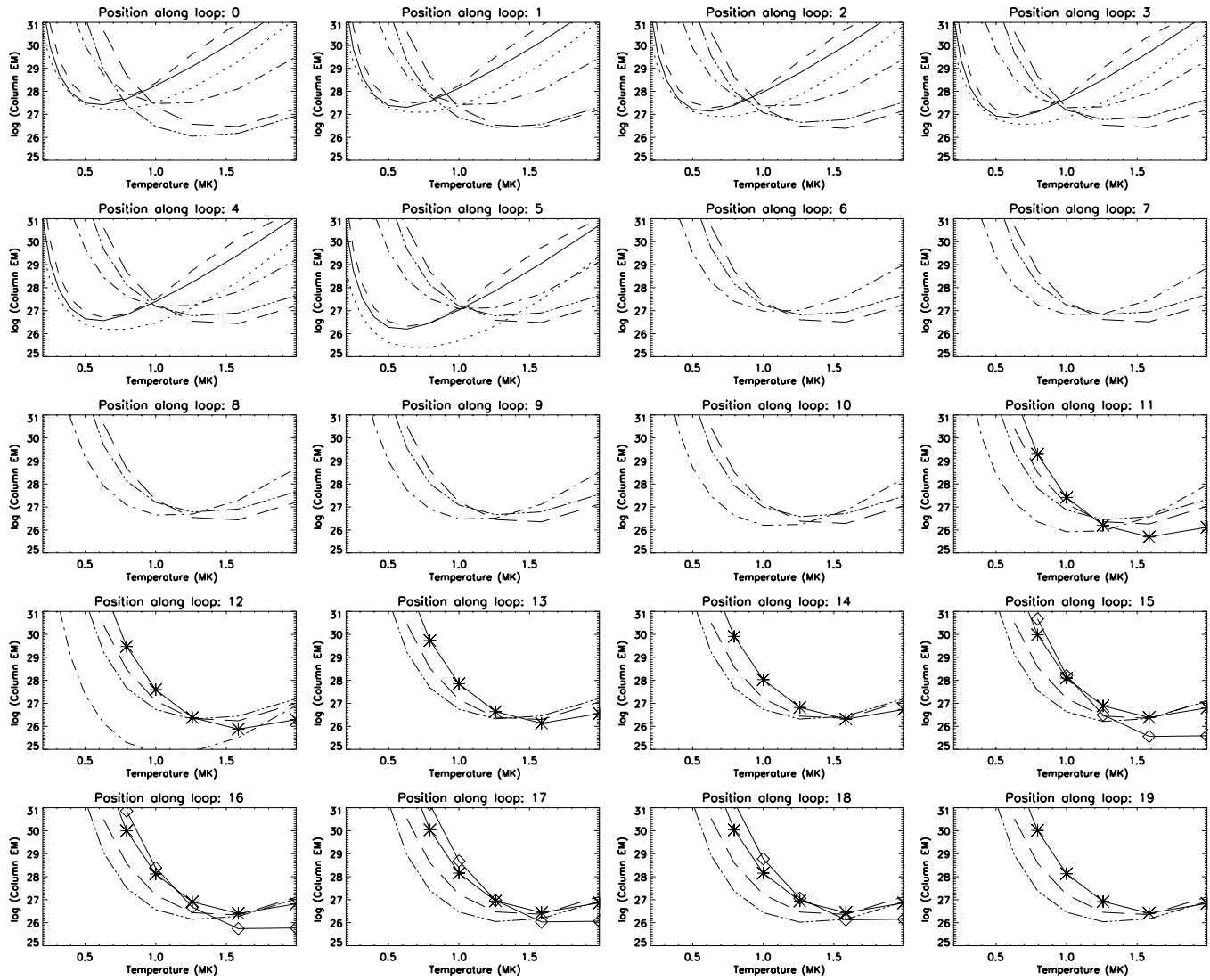


Figure 6. Emission measure curves obtained from the background-subtracted line intensities for loop A. Different plots correspond to different data points chosen along the loops. In the plots, the solid lines represent the EM-loci of Si VII, dotted lines Fe VIII, dashed lines Mg VII, dashed–dotted Fe X, dashed–triple dotted Fe XII, and long-dashed lines represent Si X. The solid lines overplotted with asterisks and diamonds represent the EM-loci of Fe XIII and Fe XIV, respectively. The emission measure was calculated using Arnaud & Rothenflug (1985) ionization fraction and coronal abundances of Feldman (1992).

slightly to the east and labeled BG in Figure 5. We chose this location to avoid the eruptive material which might contaminate the background emission to the west of the active region. Furthermore, we have smoothed out the intensity along the loop and background intensity before subtraction to avoid any local fluctuations. It is worth mentioning here that we selected different regions for background subtraction and the results were similar with a difference of about 5%–10%.

Figure 6 displays the EM-loci plots for loop A measured at points (1–20, point 1 being at the footpoint and 20th toward the loop top) along the loops shown in Figure 5, from south to north. The EM-loci plots clearly demonstrate that the coronal loop studied here is nearly isothermal along the LOS and the temperature increases along the loop. Close to the footpoints of the loop the temperature is ≈ 0.8 MK and increases to ≈ 1.5 MK at the projected height of about 75 Mm. For the first few points (toward the loop footpoint), the EM-loci for Fe VIII are not consistent with other lines. The discrepancy is due to a problem with the atomic data for Fe VIII (Del Zanna et al. 2003). A similar trend is found for loop B.

3.4. Electron Density and Filling Factor Along Coronal Loops

In order to derive electron densities along the loop we have selected several diagnostic line pairs such as Mg VII $\lambda 280$ and $\lambda 278$, Si X $\lambda 258$ and $\lambda 261$, and Fe XII $\lambda 186$ and $\lambda 195$ (Young et al. 2007b). The electron density values were obtained using the theoretical line intensity ratios calculated using CHIANTI version 5.2 (Dere et al. 1997; Landi et al. 2006). However, we note that the Mg VII $\lambda 278$ and Fe XIV $\lambda 274$ lines are blended with Si VII lines and therefore we have used the Si VII $\lambda 275$ line, which is a strong line, to remove the blend. The two Fe XII lines are self-blended and care must be taken while deriving densities using Fe XII line ratios.

Figure 5 shows the intensity image obtained in Fe X $\lambda 184$ line overplotted with asterisks showing selected pixels along the loops and the background. In order to obtain a valid electron density for a coronal loop, it is necessary to subtract the background intensities. It has been shown that the results can be significantly different if a proper background subtraction is not performed (see, e.g., Del Zanna & Mason 2003). Note that since

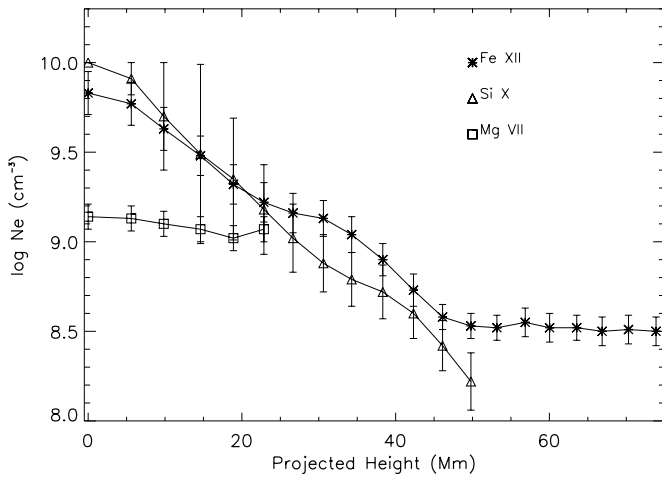


Figure 7. Variation of electron density with projected height of the loop A. Meanings of the symbols are denoted in the plot. The error bar is estimated using 10% error in the intensity.

the intensity along loop B were not significantly different from the background intensities, it was difficult to obtain accurate background-subtracted intensities for the weak diagnostic lines and to derive densities. Hence, for density and filling factor estimation we have considered only loop A.

Figure 7 shows the variation of electron density along loop A with the projected height of the loop. The squares represent the density values derived from Mg VII $\lambda(280/278)$ ($\log T[K] = 5.8$) line ratios, the asterisks represent those from Fe XII $\lambda 186/195$ ($\log T[K] = 6.1$), and the triangles are for Si X $\lambda 258/261$ ($\log T[K] = 6.1$). For Mg VII and Si X lines we did not have enough counts at higher altitudes along the loop and therefore, we could not estimate the density for the higher-loop

locations. Error bars on densities are estimated by considering a 10% error in line intensities.

It is immediately evident from Figure 7 that the electron densities decrease with altitude along the loop for Fe XII and Si X. However, for Mg VII it does not show as sharp a decrease. The densities obtained from Fe XII and Si X are within the consistent error bar. Note that for Fe XII the results are based on the atomic calculation by Storey et al. (2005). The electron densities obtained using Mg VII are significantly different. In fact, the densities using these lines could be only measured toward the footpoint location. At the projected height of about 20 Mm the densities using Mg VII become similar to those of Fe XII and Si X.

Another important parameter to determine is the filling factor (defined by Equation (3)) for coronal loops. This is an indicator of whether loop structures are composed of multiple strands or not (Cargill & Klimchuk 1997). The most problematic parameter in the filling factor calculation is the thickness of the loop along the LOS. In this study, we have considered the diameter of the loop to be equivalent to the thickness. The loop's diameter measured using Fe XII image was used as thickness when estimating the filling factors using Fe XII and Si X lines. The loops, however, in transition region lines such as Mg VII appear to be thicker toward the footpoint. We have measured the width of the loops using the image obtained in Mg VII $\lambda 278$ and used this as the thickness along the LOS for the filling factor calculation using Mg VII densities.

Table 1 provides from left to right: the projected height of the loop, the thickness (diameter) of the loop along the LOS, electron densities, filling factors, and the path length for the three ions such as Fe XII, Si X, and Mg VII. The filling factors for Fe XII densities are about 0.02 at the footpoint and about 0.8 at a projected height of 40 Mm. For Si X lines, the filling factors

Table 1
Derived Parameters Along the Loop A Using Fe XII, Si X, and Mg VII Lines

Projected Height (Mm)	Fe XII				Si X			Mg VII			
	h (")	N_e (cm s^{-3})	ϕ	d (")	N_e (cm s^{-3})	ϕ	d (")	h (")	N_e (cm s^{-3})	ϕ	d (")
0	7	9.83	0.02	0.18	10.00	0.00	0.02	20	9.14	1.79	37.69
5	8	9.77	0.02	0.22	9.91	0.01	0.10	17	9.13	1.71	30.40
9	6	9.63	0.06	0.36	9.70	0.06	0.44	15	9.10	1.48	23.33
14	10	9.48	0.07	0.77	9.49	0.14	1.47	15	9.07	0.84	13.16
18	10	9.32	0.15	1.59	9.35	0.26	2.78	15	9.02	0.56	8.78
22	13	9.22	0.20	2.69	9.18	0.43	5.93	10	9.07	0.28	2.91
26	12	9.16	0.29	3.71	9.02	1.03	12.99
30	11	9.13	0.37	4.32	8.88	2.11	24.41
34	11	9.04	0.47	5.48	8.79	2.86	33.08
38	10	8.90	0.79	8.30	8.72	3.25	34.17
42	11	8.73	1.30	15.06	8.60	4.14	47.81
46	10	8.58	2.63	27.65	8.42	7.40	77.62
49	7	8.53	4.52	33.19	8.22	18.73	137.54
53	12	8.52	3.11	39.26
56	10	8.55	3.66	38.38
60	10	8.52	4.21	44.12
63	9	8.52	4.57	43.12
66	11	8.50	4.41	50.88
70	12	8.51	3.80	47.87
73	12	8.50	3.89	48.94

Notes. In this table, " h " is the diameter of the loop in arcsec, " N_e " is the electron density, " ϕ " is the filling factor, and " d " is the path length. The measured diameter was used as the thickness of the loop along the LOS. Note that the same values of " h " as Fe XII were used while deriving filling factors using Si X line. We have used coronal abundances of Feldman (1992).

were similar to those of Fe XII lines but become more than 1 at a projected height of 25 Mm. We believe that this is because of the less reliable densities obtained using Si X lines ratios. We find substantially different results for Mg VII with a filling factor close to 1. For Mg VII, the filling factor decreases with altitude giving reliable values only up to around 15 Mm. The filling factor values using Mg VII lines were close to 1 similar to the *SOHO*/CDS measurements using Mg VII lines (see Del Zanna 2003; Del Zanna & Mason 2003).

4. SUMMARY AND CONCLUSIONS

The EIS on board *Hinode* provides an excellent opportunity to study the physical plasma properties over a range of temperatures simultaneously in spatially resolved coronal structures. This is extremely important when studying the problem of active region heating. In this paper, we have studied the overall temperature structure and flows in an active region and in a particular spatially resolved coronal loop. In addition, we have also derived densities and filling factors along this loop. The main results are summarized below.

1. The high-lying loop structures are seen more distinctly in the images obtained using lower-temperature lines. With increasing temperature the core of the active region becomes more apparent and the overall structure becomes fuzzier. The active region is comprised throughout of upflows and downflows. The downflows are predominantly seen in the core of the active region. However, the upflows are seen at the boundary of the active region in the low-emission regions. With increasing temperature the regions showing redshifted emission in low temperature at the boundary of active region turns toward blueshifted emission (see Figures 2 and 3).
2. In a well-resolved coronal loop we observed downflows (redshifts) along the loop at all temperatures. The downflows are seen only toward the footpoint in Si VII and are very strong, $\approx 60 \text{ km s}^{-1}$. However, in Fe X and Fe XII downflows are seen all along the loop being stronger toward the footpoint. In high-temperature lines such as Fe XIV and Fe XV the downflows are localized toward the loop top (see Figure 2). We note that the velocities measured at quiet Sun vary with temperature (Peter & Judge 1999). Taking account of this variation would not substantially affect our results.
3. The active region structures are more clearly defined in lower-temperature lines and appear “fuzzy” at higher temperature. This is consistent with indications from previous solar observations. However, confirmation of this required spectroscopic observations with the same instrument over a range of temperatures, with good spatial resolution, is provided by the EIS (see Figure 4).
4. Using the EM-loci method we find that both loops studied here are almost isothermal along the LOS. The temperature at the footpoint is about 0.80 MK and increases to about 1.5 MK at a projected height of about 75 Mm (see Figure 6).
5. The derived electron densities decrease with loop altitude. Toward the footpoint, the electron density estimated using Fe XII ratios is $\log N_e = 9.8 \text{ cm}^{-3}$ which decreases to $\log N_e = 8.5 \text{ cm}^{-3}$ at an altitude of about 75 Mm. The densities obtained using Si X were similar to Fe XII densities. However, the estimated densities using Mg VII line ratios were smaller than those obtained using Fe XII toward the footpoint locations and reached a value similar to that of Fe XII at a projected height of about 25 Mm (see Figure 7).
6. Using the densities obtained by Fe XII, Si X, and Mg VII line ratios and the loop’s diameter as the thickness along the LOS, we find that the filling factor increases with the projected height. The filling factor obtained using Fe XII densities is about 0.02 at the footpoint and about 0.8 at a projected height of 40 Mm. For Si X lines, the filling factors were similar to those of Fe XII lines but become more than 1 at a projected height of 25 Mm. We find substantially different results for Mg VII (see Table 1), closer to unity.

5. DISCUSSION

An understanding of the problem of the coronal heating is a long-lasting one and it is now widely believed that studying the physics of all kinds of loops holds the key. There have been many recent theoretical developments to explain the heating in coronal loops and in active regions. However, the observational confirmations of these theories have not been possible unambiguously for various reasons. For example, the “nanoflare” model originally proposed by Parker (1988) and later on globally modeled by Cargill (1994) (see also Kopp & Poletto 1993) suggests that the coronal loops are comprised of many subresolution strands and they are all being heated separately. This predicts that the loops are multithermal along the LOS. In addition, this model also predicts high-velocity evaporative upflows at high temperatures. Using the idea of multistranded coronal loops in a one-dimensional hydrodynamic simulation, Patsourakos & Klimchuk (2006) suggested that these high-velocity upflows can be seen as a nonthermal broadening with a particular enhancement in blue wing in high-temperature spectral lines. Observational confirmation of these predictions can only be unambiguously performed using spectroscopic observations with high spectral and spatial resolution with a broad temperature coverage.

Thanks to the excellent simultaneous spectral and spatial resolution of EIS, we are now able to study flows and other physical parameters in an active region and also in spatially resolved coronal structures in detail. Observations of strong downflows at the footpoint in cooler transition region temperatures are similar to previous observations using SUMER measurements (see, e.g., Peter & Judge 1999; Teriaca et al. 1999). In addition to that we also observed downflows only toward the loop top in higher-temperature lines such as Fe XIV and Fe XV. The observation of downflows at all temperatures raises the question concerning the origin of the plasma in the loop and suggests that there must be some sort of upflow of plasma filling up the loops. Patsourakos & Klimchuk (2006) performed a forward modeling of Fe XVII emission line for EIS using data from one-dimensional hydrodynamic simulations and suggested that the signatures of high-speed upflows can be seen as nonthermal broadening and blue-wing enhancement in the Fe XVII line observed by the EIS. Unfortunately, the study sequence used in the present analysis did not contain that line with sufficient counts preventing us to perform a direct comparison. Recently, Hara et al. (2008) studied line profiles for Fe XV at footpoint of coronal loops. They observed a slight enhancement in the blue wing suggesting that this could be associated with high-velocity upflows at higher temperature as suggested by Patsourakos & Klimchuk (2006). Similar to our observations, Hara et al. (2008) also did not observe any signature of downflows toward the footpoint of the loops in high-temperature lines and suggested that the ab-

sence of downflows toward the footpoint could be attributed to the presence of high-velocity upflows. Moreover, in the present study the observations of average flow structures turning from downflows to upflows in regions located at the footpoints of the coronal loops provide another argument in favor of upflows in coronal loops at higher temperatures. In a recent study, using the idea of nanoflare footpoint heating, Antolin et al. (2008) predict upflows of plasma in Fe xv line which seem to match with our observations.

The idea of multistranded impulsively heated coronal loop suggests that the filling factor values should be less than unity. This is precisely what our measurements show. In our measurements, we find that the filling factors are much less than unity at $\log T[\text{MK}] = 6.1$ and is closer to unity at transition region temperature ($\log T[\text{MK}] = 5.8$) toward the footpoint. However, with increasing projected height, the filling factors at $\log T[\text{MK}] = 6.1$ increase while that for $\log T[\text{MK}] = 5.8$ decrease. This means that toward the footpoints of the loop most of the plasma is at transition region temperature. However, with increasing projected height, the amount of plasma at $\log T[\text{MK}] = 6.1$ increases. This suggests an increasing temperature with projected height of the loop. This is exactly what we obtained using the EM-loci analysis. The EM-loci analysis (see Figure 6) shows that the temperature along the loop increases with the projected height of the loop being ≈ 0.8 MK at the footpoint and ≈ 1.5 MK at a projected height of about 75 Mm.

The EM-loci analysis also shows that the plasma along the LOS is close to isothermal. However, the different flow structures and densities obtained using different spectral lines and filling factors values less than unity emphasize the multithermality of the plasma along the LOS. It is not trivial to reconcile these two results together. We note that the multithermality of plasma along the LOS is one of the most important ingredient in the model of multistranded impulsively heated coronal loop. However, so far we do not know how multithermal or how isothermal the plasma is observationally and also theoretically. In this analysis, e.g., at least for the first few points from the footpoint of the loop, the loops do not appear to be exactly isothermal. There appears a narrow distribution of temperatures. Based on observations of a number of loops using EIS data, Warren et al. (2008) showed that the coronal loops which are bright at Fe xii have a narrow distribution of temperature but they are not isothermal.

The observations of high-speed downflows and concurrent upflows in coronal loops in addition to very low values of filling factors and their nearly isothermal structure along the LOS provide very important constraints in the modeling of coronal loops. Given the capabilities of EIS, more measurements should be performed for many other coronal loops to obtain more statistically accurate values of these parameters.

We thank the referee for constructive comments. D.T., H.E.M., and G.D.Z. acknowledge STFC. B.N.D. acknowledges HEM for support through a rolling grant from STFC at DAMTP. *Hinode* is a Japanese mission developed and launched by ISAS/JAXA, collaborating with NAOJ as a domestic partner, NASA and STFC (UK) as international partners. Scientific operation of the *Hinode* mission is conducted by the *Hinode* science team organized at ISAS/JAXA. This team mainly consists of scientists from institutes in the partner countries. Support for the post-launch operation is provided by JAXA and NAOJ (Japan), STFC (UK), NASA, ESA, and NSC (Norway).

REFERENCES

- Antolin, P., Shibata, K., Kudoh, T., Shiota, D., & Brooks, D. 2008, *ApJ*, **688**, 669
- Arnaud, M., & Rothenflug, R. 1985, *A&AS*, **60**, 425
- Aschwanden, M. J., Schrijver, C. J., & Alexander, D. 2001, *ApJ*, **550**, 1036
- Cargill, P. J. 1994, *ApJ*, **422**, 381
- Cargill, P. J., & Klimchuk, J. A. 1997, *ApJ*, **478**, 799
- Cirtain, J. W., et al. 2007, *ApJ*, **655**, 598
- Culhane, J. L., et al. 2007, *Sol. Phys.*, **243**, 60
- Curd, W., Tian, H., Dwivedi, B. N., & Marsch, E. 2008, *A&A*, **491**, 13
- Dammasch, I. E., Curdt, W., Dwivedi, B. N., & Parenti, S. 2008, *Ann. Geophys.*, **26**, 2955
- Del Zanna, G. 2003, *A&A*, **406**, L5
- Del Zanna, G. 2008a, in ASP Conf. Ser. 397, *Announcing First Results from Hinode*, ed. S. Mathews et al. (San Francisco, CA: ASP), 87
- Del Zanna, G. 2008b, *A&A*, **481**, L49
- Del Zanna, G., Bromage, B. J. I., & Mason, H. E. 2003, *A&A*, **398**, 743
- Del Zanna, G., Landini, M., & Mason, H. E. 2002, *A&A*, **385**, 968
- Del Zanna, G., & Mason, H. E. 2003, *A&A*, **406**, 1089
- Del Zanna, G., & Mason, H. E. 2005a, *A&A*, **433**, 731
- Del Zanna, G., & Mason, H. E. 2005b, *Adv. Space Res.*, **36**, 1503
- Del Zanna, G., Mason, H. E., & Cirtain, J. 2006, in Proc. *SOHO-17, 10 Years of SOHO and Beyond*, ed. H. Lacoste & L. Ouweland (Noordwijk: ESA), 617
- Dere, K. P., Landi, E., Mason, H. E., Monsignori Fossi, B. C., & Young, P. R. 1997, *A&AS*, **125**, 149
- Dere, K. P., & Mason, H. E. 1981, in *Solar Active Regions: A Monograph from Skylab Solar Workshop III*, ed. F. Q. Orall (Boulder, CO: Colorado Assoc. Univ. Press), 129
- Domingo, V., Fleck, B., & Poland, A. I. 1995, *Sol. Phys.*, **162**, 1
- Doschek, G. A., et al. 2008, *ApJ*, **686**, 1362
- Feldman, U. 1992, *Phys. Scr.*, **46**, 202
- Handy, B. N., et al. 1999, *Sol. Phys.*, **187**, 229
- Hara, H., Watanabe, T., Harra, L. K., Culhane, J. L., Young, P. R., Mariska, J. T., & Doschek, G. A. 2008, *ApJ*, **678**, L67
- Harra, L. K., Sakao, T., Mandrini, C. H., Hara, H., Imada, S., Young, P. R., van Driel-Gesztelyi, L., & Baker, D. 2008, *ApJ*, **676**, L147
- Harrison, R. A., et al. 1995, *Sol. Phys.*, **162**, 233
- Klimchuk, J. A. 2006, *Sol. Phys.*, **234**, 41
- Kopp, R. A., & Poletto, G. 1993, *ApJ*, **418**, 496
- Landi, E., Del Zanna, G., Young, P. R., Dere, K. P., Mason, H. E., & Landini, M. 2006, *ApJS*, **162**, 261
- Marsch, E., Tian, H., Sun, J., Curdt, W., & Wiegmann, T. 2008, *ApJ*, **685**, 1262
- Mason, H. E., Landi, E., Pike, C. D., & Young, P. R. 1999, *Sol. Phys.*, **189**, 129
- Mason, H. E., & Monsignori Fossi, B. C. M. 1994, *A&AR*, **6**, 123
- Mazzotta, P., Mazzitelli, G., Colafrancesco, S., & Vittorio, N. 1998, *A&AS*, **133**, 403
- Milligan, R. O., Gallagher, P. T., Mathioudakis, M., Keenan, F. P., & Bloomfield, D. S. 2005, *MNRAS*, **363**, 259
- Narain, U., & Ulmschneider, P. 1996, *Space Sci. Rev.*, **75**, 453
- Parker, E. N. 1988, *ApJ*, **330**, 474
- Patsourakos, S., & Klimchuk, J. A. 2006, *ApJ*, **647**, 1452
- Peter, H., & Judge, P. G. 1999, *ApJ*, **522**, 1148
- Porter, L. J., & Klimchuk, J. A. 1995, *ApJ*, **454**, 499
- Schmelz, J. T., Nasraoui, K., Del Zanna, G., Cirtain, J., DeLuca, E. E., & Mason, H. E. 2007, *ApJ*, **658**, 119
- Schmelz, J. T., Scopes, R. T., Cirtain, J. W., Winter, H. D., & Allen, J. D. 2001, *ApJ*, **556**, 896
- Storey, P. J., Del Zanna, G., Mason, H. E., & Zeppen, C. J. 2005, *A&A*, **433**, 717
- Teriaca, L., Banerjee, D., & Doyle, J. G. 1999, *A&A*, **349**, 636
- Tripathi, D., Mason, H. E., & Young, P. R. 2006, *SOHO-17, Vol. 617, 10 Years of SOHO and Beyond*, ESA Special Publication, (Noordwijk: ESA)
- Tripathi, D., Mason, H. E., Young, P. R., Chifor, C., & Del Zanna, G. 2008a, in ASP Conf. Ser. 397, *Announcing First Results from Hinode*, ed. S. Mathews et al. (San Francisco, CA: ASP), 45
- Tripathi, D., Mason, H. E., Young, P. R., & Del Zanna, G. 2008b, *A&A*, **481**, L53
- Tsuneta, S., et al. 1991, *Sol. Phys.*, **136**, 37
- Warren, H. P., Ugarte-Urra, I., Doschek, G. A., Brooks, D. H., & Williams, D. R. 2008, *ApJ*, **686**, 131
- Young, P. R., Del Zanna, G., Mason, H. E., Doschek, G. A., Culhane, L., & Hara, H. 2007a, *PASJ*, **59**, 727
- Young, P. R., Watanabe, T., Hara, H., & Mariska, J. T. 2009, *A&A*, **495**, 587
- Young, P. R., et al. 2007b, *PASJ*, **59**, 857